

Article

Microcrack Porosity Estimation Based on Rock Physics Templates: A Case Study in Sichuan Basin, China

Chuantong Ruan ^{1,2}, Jing Ba ^{1,*}, José M. Carcione ^{1,3}, Tiansheng Chen ⁴ and Runfa He ¹

¹ School of Earth Sciences and Engineering, Hohai University, Nanjing 211100, China; rct@hhu.edu.cn (C.R.); jcarcione@libero.it (J.M.C.); herunfa@hhu.edu.cn (R.H.)

² School of Mathematics and Statistics, Zhoukou Normal University, Zhoukou 466001, China

³ National Institute of Oceanography and Applied Geophysics (OGS), 34010 Trieste, Italy

⁴ Petroleum Exploration and Production Research Institute, SINOPEC, Beijing 100083, China; chents.syky@sinopec.com

* Correspondence: jba@hhu.edu.cn

Abstract: Low porosity-permeability structures and microcracks, where gas is produced, are the main characteristics of tight sandstone gas reservoirs in the Sichuan Basin, China. In this work, an analysis of amplitude variation with offset (AVO) is performed. Based on the experimental and log data, sensitivity analysis is performed to sort out the rock physics attributes sensitive to microcrack and total porosities. The Biot–Rayleigh poroelasticity theory describes the complexity of the rock and yields the seismic properties, such as Poisson’s ratio and P-wave impedance, which are used to build rock-physics templates calibrated with ultrasonic data at varying effective pressures. The templates are then applied to seismic data of the Xujiahe formation to estimate the total and microcrack porosities, indicating that the results are consistent with actual gas production reports.

Keywords: tight sandstone gas reservoirs; rock-physics template; Biot–Rayleigh theory; total porosity; microcrack porosity



Citation: Ruan, C.; Ba, J.; Carcione, J.M.; Chen, T.; He, R. Microcrack Porosity Estimation Based on Rock Physics Templates: A Case Study in Sichuan Basin, China. *Energies* **2021**, *14*, 7225. <https://doi.org/10.3390/en14217225>

Academic Editors: Joel Sarout and Manoj Khandelwal

Received: 23 August 2021

Accepted: 27 October 2021

Published: 2 November 2021

Publisher’s Note: MDPI stays neutral with regard to jurisdictional claims in published maps and institutional affiliations.



Copyright: © 2021 by the authors. Licensee MDPI, Basel, Switzerland. This article is an open access article distributed under the terms and conditions of the Creative Commons Attribution (CC BY) license (<https://creativecommons.org/licenses/by/4.0/>).

1. Introduction

The development of society has led to a significant increase in the demand of oil and gas resources, and the depletion of conventional petroleum resources made the exploration and extraction of unconventional hydrocarbon resources necessary [1,2]. Tight sandstone reservoirs are widely distributed and account for a high production of China’s total natural gas [3,4]. Large-scale gas fields with great potential have been discovered in more than ten basins, including Sichuan, Ordos, Songliao, Tuha, and Junggar [5].

Deep burial generally leads to high mechanical compaction and cementation of a sandstone reservoir, so that tight and heterogeneous reservoir rocks are generated, where microcracks are developed [6]. These microcracks affect the rock elastic properties and control the fluid flow, providing channels for hydrocarbon migration [7–9]. Their identification is a key factor for evaluating reservoir quality [10,11].

The study of microcracks in tight sandstones has become an important topic of rock-physics studies [12]. Hudson [13] established a relation between microcrack density and rock elastic properties, while Smith [14] stated that in low porosity rocks, the effect of cracks on seismic velocity can be important as mineral composition, total porosity, and fluid type. Yoon [15] established a relation between aspect ratio and microcrack density. Cheng [16] studied the effect of effective pressure and fluids. Zhang et al. [17,18] proposed a differential poroelastic model to describe wave propagation and dissipation in fluid-saturated rocks which contain inclusions at multiple scales.

The use of RPT (rock physics template; the list of abbreviations is given in Abbreviations) is widespread: Avseth and Ødegaard [19] linked the reservoir characteristics with elastic attributes, whereas Avseth et al. [20] used the Biot–Gassmann theory to discriminate

between oil and gas in reservoirs. RPT was also used by Xin and Han [21] to estimate reservoir lithology and fluids. Michel [22] predicted porosity and oil saturation in shales, based on RPTs built with P-wave impedance (I_P) and the ratio between the P- and S-wave velocities (V_P/V_S). Gupta et al. [23] identified thin sandy layers saturated with oil, and Ba et al. [24] estimated porosity and gas saturation. Carcione and Avseth [25] evaluated organic content, hydrocarbon saturation, and in-situ pressure in source rocks, and Liu et al. [26] proposed a combination of fluid indicators. Pang et al. [27] predicted microcrack properties in tight sandstone reservoirs, based on P-wave impedance and attenuation.

The Biot–Rayleigh (BR) theory was introduced by Ba et al. [28,29] for describing wave propagation characteristics in rocks with multi-phase pore structures. This work is mainly based on BR theory. We consider ten wells in the proposed area and perform a sensitivity analysis by using the ultrasonic and well-log data. On the basis of Poisson’s ratio (ν) and P-wave impedance, we establish multi-scale RPTs for tight sandstone gas reservoirs, which relate the total and microcrack porosities to the seismic properties, which are obtained by means of seismic inversion.

2. Overview of the Work Area

2.1. Geology

The West Sichuan depression, bounded by the Longmenshan thrust and Longquanshan uplift belts, is a key area of natural gas exploration in China [30]. The maximum buried depth of the Xujiahe Formation exceeds 4.5 km, and the average thickness of the target layer is approximately 120 m. The work area was subjected to multi-stage Indosinian, Yanshan, and Himalayan tectonic movements, which resulted in diverse structural fractures that are controlled by complex diagenesis processes. A mechanical compaction is an aspect of diagenesis that destroys the primary pores. The sedimentary facies are mainly about the braided river delta facies. The channels overlap with each other from different periods, forming a longitudinal superposition and plane contiguous sand bodies [31].

2.2. Reservoir Characteristics

The tight sandstones are mainly composed of litharenites, with small amounts of lithic quartz arenite and feldspathic litharenite. In terms of mineral content, the average amounts of quartz and feldspar are 69% and 8.2%, respectively [32]. The effect of compaction on the reservoirs is more significant than that of cementation. Figure 1 shows that the compaction process is responsible for the developed geological characteristics such as complex pore structures and network microcracks. The average secondary, primary, and microcrack porosities are 2.9%, 1.1%, and 0.3%, respectively. The grain size varies from fine to medium, and the sorting property varies from poor to good. Moreover, the reservoir exhibits low porosity, low matrix permeability, and small pore-throat radii [31]. The microcracks maintain the reservoir connectivity and facilitate the gas production [33].

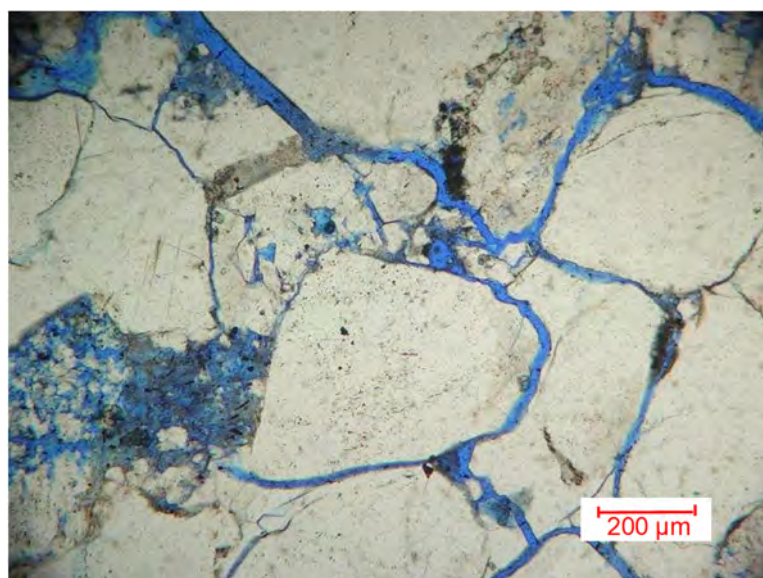


Figure 1. Thin section of a tight sandstone showing microcracks and a complex pore structure.

2.3. AVO Characteristics

Amplitude variations with offset (AVO) discriminate lithologies and help to detect hydrocarbons [34]. Rutherford and Williams [35] categorized the AVO responses of mudstone/gas-bearing sandstone interface into the three types. Subsequently, Castagna and Swan [36] added a fourth AVO response type. We analyze the AVO characteristics based on the profiles of Well P, shown in Figure 2, where the target layer is indicated with dashed red lines. Table 1 shows the seismic properties of the sandstone model of the Xujiahe Formation based on the log data. To obtain the P- and S-wave velocities and density, a 60 m interval is selected. The model data are collected from the interval above the top interface of the target layer that has a relatively stable P-wave velocity. For the target layer, we consider average values.

Figure 3 illustrates the AVO of the top (red color) and bottom (blue color) interfaces. The characteristics of the curves agree with the fact that the P- and S-wave impedances of the target layer are smaller than those of the overburden mudstone. The top and bottom responses are type IV and I AVO curves, respectively.

Table 1. Seismic properties, corresponding to the sandstone model of the Xujiahe Formation.

Well	Top			Target Layer			Bottom		
	V_p (m/s)	V_s (m/s)	Density (g/cm ³)	V_p (m/s)	V_s (m/s)	Density (g/cm ³)	V_p (m/s)	V_s (m/s)	Density (g/cm ³)
P	4453	2812	2.5360	3956	2462	2.5298	4787	2983	2.5531

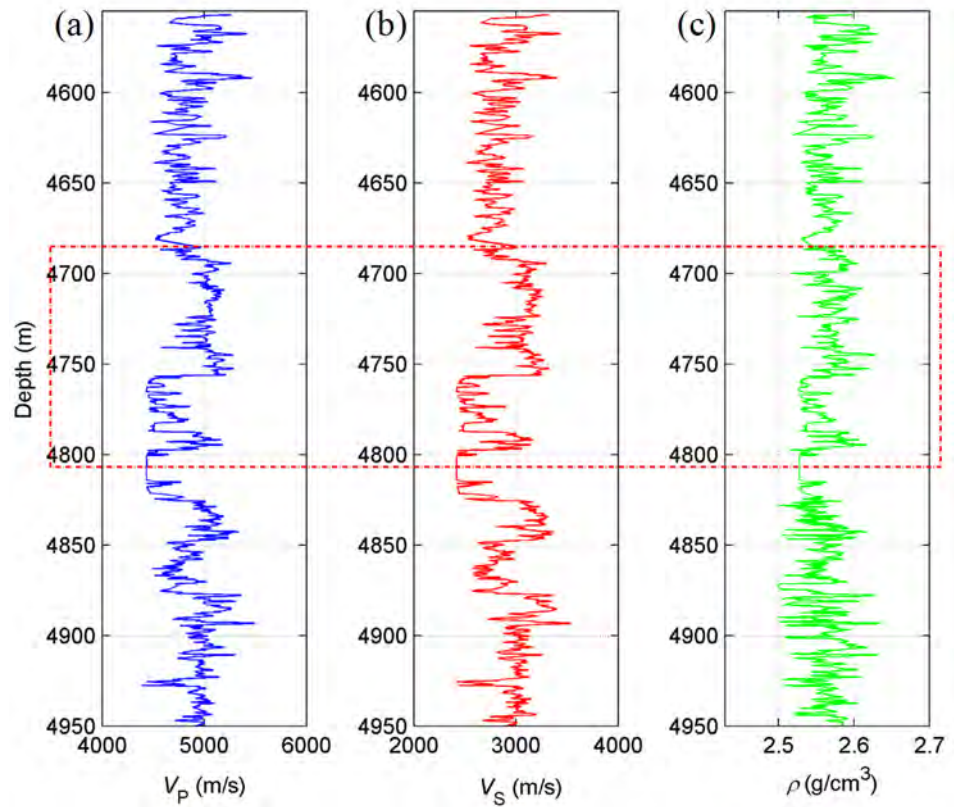


Figure 2. Log profiles of Well P. (a) P-wave velocity, (b) S-wave velocity, and (c) density.

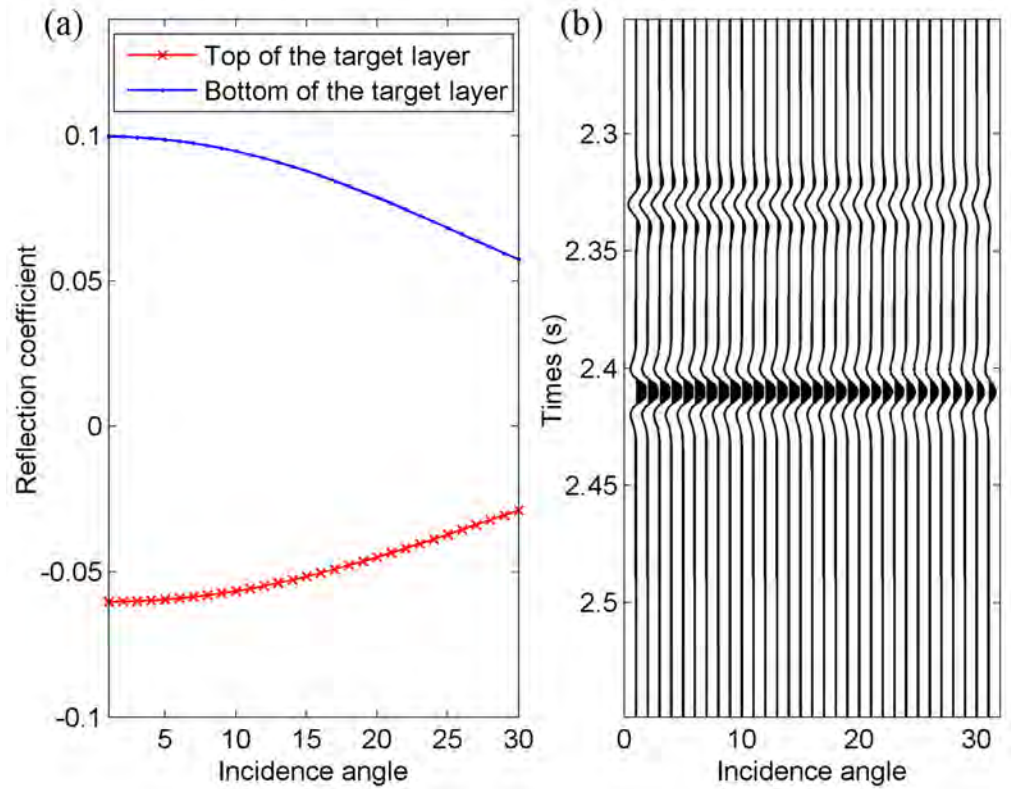


Figure 3. (a) AVO curves and (b) synthetic seismic records of the target layer.

3. Theory and Flowchart

Figure 4 shows an idealization of the tight sandstone of the Xujiache Formation, which is characterized by a complex pore structure and microcrack network. The total porosity is the sum of intergranular and microcrack porosity.

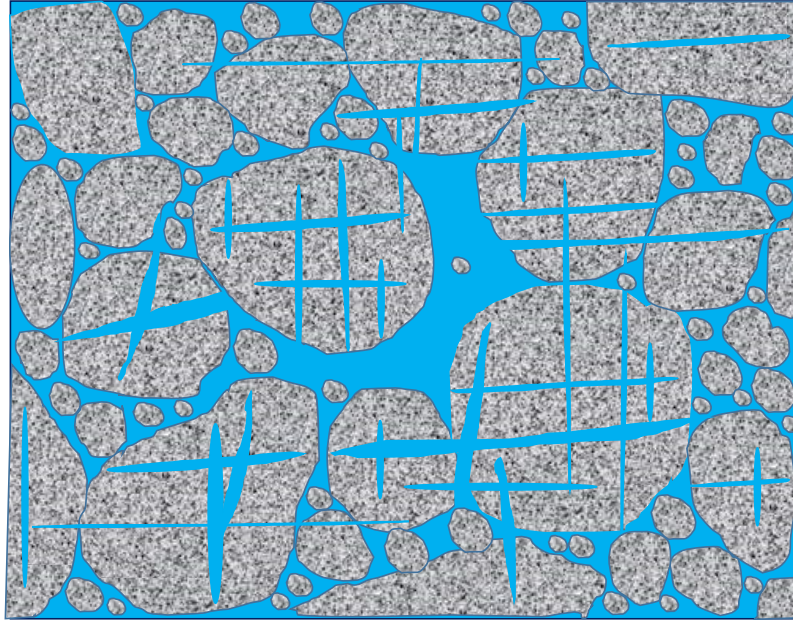


Figure 4. Scheme of tight sandstone pore structure with intergranular pores and microcrack network.

The flowchart for the prediction of the reservoir properties is given in Figure 5. The microcrack porosity is estimated by using the quantitative relation between the elastic attributes and reservoir properties, based on a rock-physics model and aided by geological, log data, and ultrasonic data.

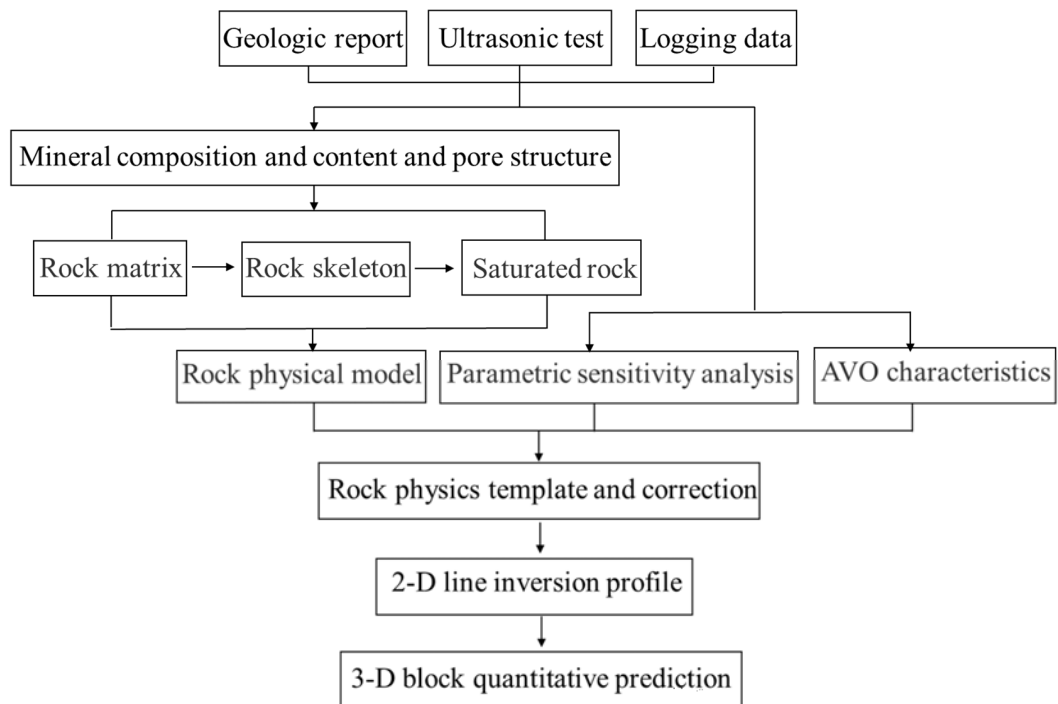


Figure 5. Flowchart for the prediction of the reservoir properties.

The main minerals are quartz, feldspar, and clay. The total porosity is less than 12%. The procedure to establish the rock-physics model is as follows.

- (1) The Voigt–Reuss–Hill equation [37–39] is used to compute the elastic modulus of mineral mixture M_{VRH} according to the mineral composition:

$$M_V = \sum_{i=1}^N f_i M_i, \quad (1)$$

$$\frac{1}{M_R} = \sum_{i=1}^N f_i / M_i, \quad (2)$$

$$M_{VRH} = \frac{M_V + M_R}{2}, \quad (3)$$

where f_i and M_i denote the volume fraction and elastic modulus, respectively, of the i -th component.

- (2) According to the pore structure shown in Figure 4, we use the differential equivalent medium (DEM) theory [40] to add spherical pores and oblate cracks, whose aspect ratio are 1 and 0.0005, respectively, to add pores and microcracks into the matrix, and obtain the bulk and shear moduli of the rock skeleton (starred quantities),

$$(1 - y)d/dy[K^*(y)] = (K_2 - K^*(y))P^{(*2)}(y), \quad (4)$$

$$(1 - y)d/dy[\mu^*(y)] = (\mu_2 - \mu^*(y))Q^{(*2)}(y). \quad (5)$$

The initial conditions are $K^*(0) = K_1$ and $\mu^*(0) = \mu_1$, where K_1 and μ_1 are the bulk and shear moduli, respectively, of the initial main material (phase 1); K_2 and μ_2 are the bulk and shear moduli, respectively, of the inclusion that is gradually added (phase 2); y is the volume content of phase 2; and $P^{(*2)}$ and $Q^{(*2)}$ [41] are related to the shape of the inclusion.

- (3) The equations proposed by Batzle and Wang [42] are used to compute the bulk modulus, viscosity, and density of pore fluids at different temperatures and pressures.
- (4) The BR theory is used to compute the wave response. Appendix A shows the computation of the complex wave number k . The complex velocity is $v = \omega/k$, where ω is the angular frequency, and the P-wave velocity and quality factor are [7]

$$V_P = \left[\text{Re}(v^{-1}) \right]^{-1}, \quad (6)$$

$$Q = \frac{\text{Re}(v^2)}{\text{Im}(v^2)}, \quad (7)$$

where “Re” and “Im” take real and imaginary parts, respectively.

We consider the inclusion radius of 100 μm , and the bulk and shear moduli of the matrix are 33 GPa and 45 GPa, respectively. Gas has a bulk modulus of 0.02 GPa, a density of 0.089 g/cm^3 , and viscosity of 0.016×10^{-3} Pa·s. The crack porosity is set to 0.2%, and the total porosity varies as shown in Figure 6, where the P-wave velocity and dissipation factor are plotted as a function of frequency. Increasing porosity implies increasing velocity dispersion, attenuation, and relaxation frequency.

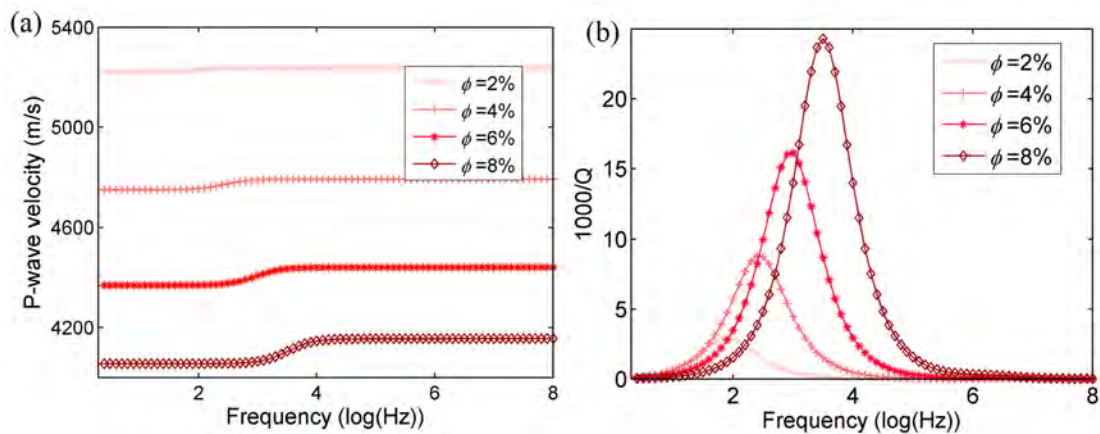


Figure 6. P-wave velocity (a) and dissipation factor (b) as a function of frequency and different total porosities.

Figure 7 shows the P- and S-wave velocities as a function of the total porosity for various microcrack porosities at 1 MHz. As can be seen, the velocities decrease with increasing total and microcrack porosities, as expected.

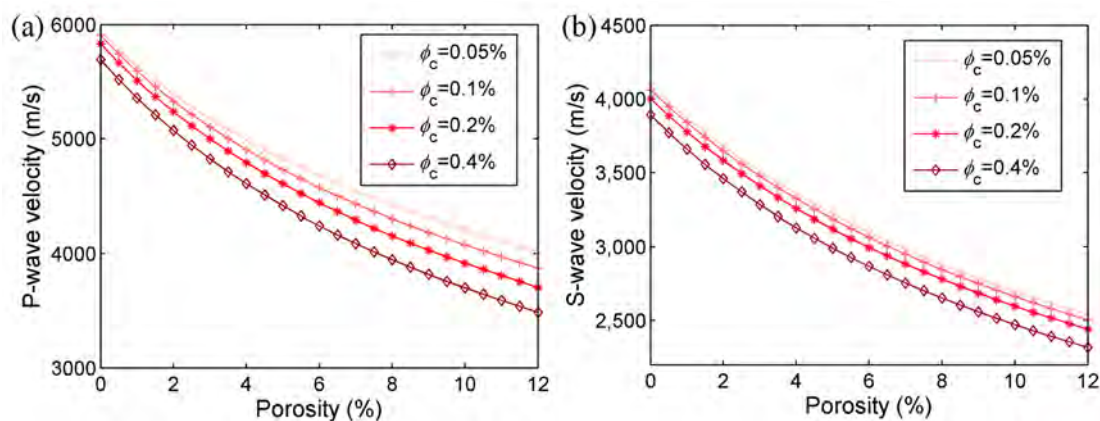


Figure 7. Effect of the total and microcrack porosities on the P-wave (a) and S-wave (b) velocities.

4. Ultrasonic Experiments and Sensitivity Analysis

To investigate the effects of the microcracks, ultrasonic experiments at 1 MHz were performed. We select a sample with a porosity of 4.39% and a grain bulk modulus of 39 MPa. The grain, dry-rock, and wet-rock densities are 2.691, 2.573, and 2.62 g/cm³, respectively, where the sample is saturated with water. The experimental setup proposed by Guo et al. [43] is used to measure the velocities at 20 °C, with the ultrasonic pulse method. The sample is sealed with a rubber sleeve and placed in the vessel. The pore pressure and temperature are fixed. Effective pressures of 5, 10, 15, 20, 25, 30, and 35 MPa are applied to the sample, in both the gas-saturated and water-saturated cases, and the velocities are measured.

As shown in Figure 8a, the measured P- and S-wave velocities increase with effective pressure. The increase of the confining pressure at a fixed pore pressure will lead to the gradual closure of internal microcracks (especially at low effective pressures), so as to stiffen the rock skeleton and increase its elastic moduli (and the wave velocities).

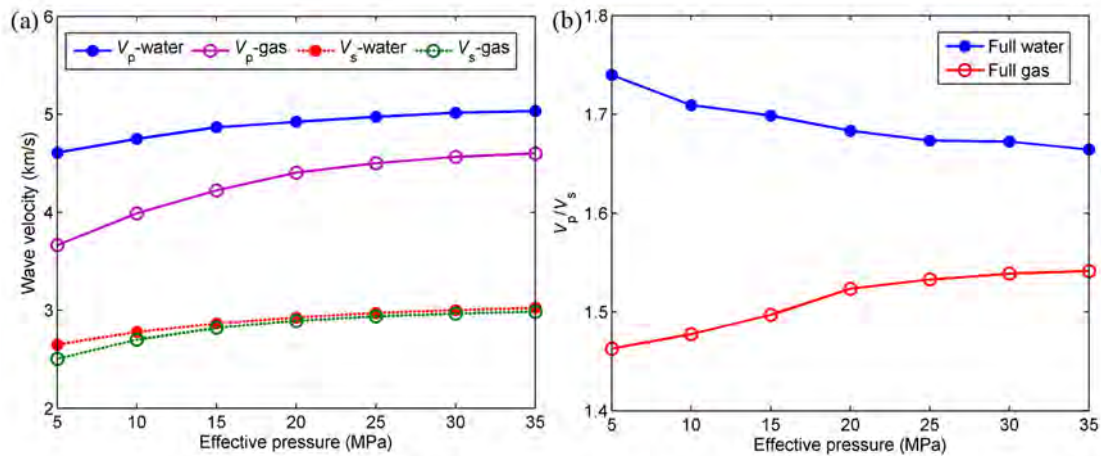


Figure 8. P- and S-wave velocities (a) and their ratio (b) as a function of effective pressure.

Figure 8b shows the velocity ratio. In the full gas saturation case, V_p/V_s increases with increasing effective pressure and the opposite behavior occurs for full water saturation case.

In addition, we measured the total porosity in the range 5–35 MPa. Microcracks with small aspect ratios tend to close first with increasing effective pressure and the relation between porosity and pressure changes from exponential to linear [44].

Experimental measurements can be performed to predict microcrack porosity based on the relation between porosity and effective pressure [45–47]. Stiff porosity can be obtained through a linear extrapolation of this relation and the microcrack porosity can be estimated as the difference between the total and stiff porosities. Figure 9 shows the different porosities as a function of the effective pressure.

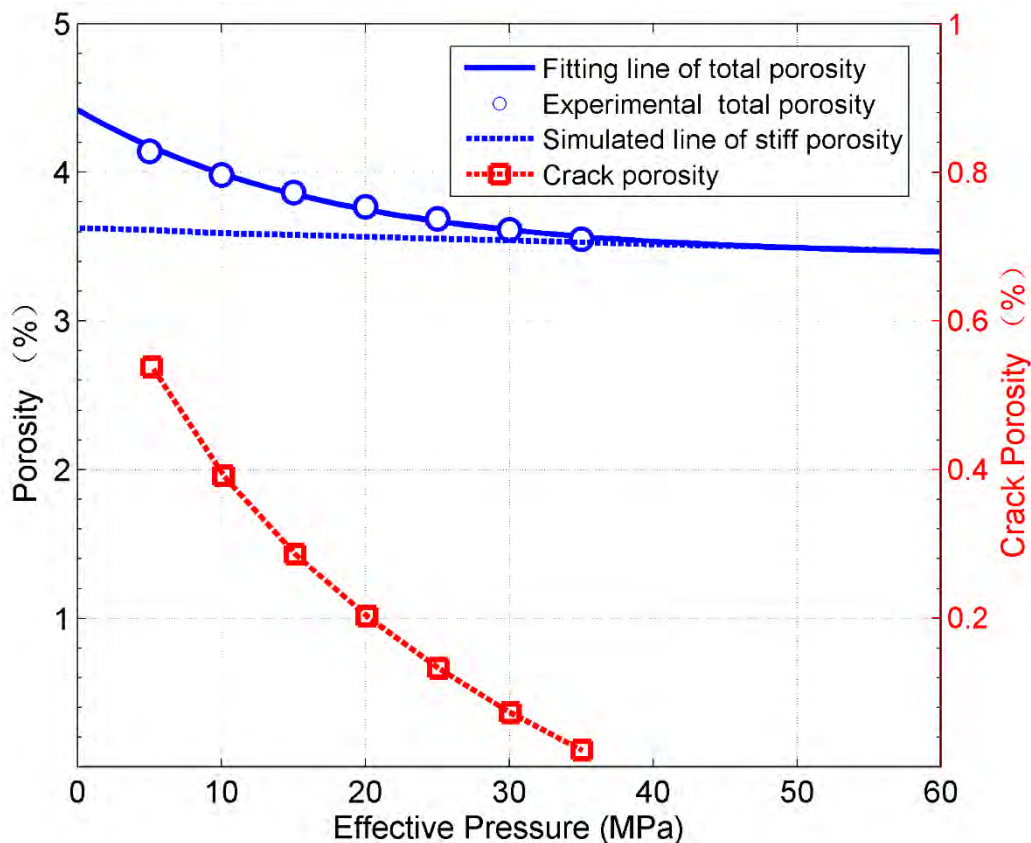


Figure 9. Total, stiff, and microcrack porosities as a function of the effective pressure.

The sensitivity analysis method like Sobol's indices can be used to analyze the interactions between the parameters, which can be applied with the given forward modeling equation or method/procedure [48]. In this work, sensitivity analysis to the total and microcrack porosities as inputs is performed based on the actually measured data from the experiments and well logs as puts, without considering the detailed modeling equations (or procedures). Based on the observed experimental or log data, the fluid sensitivity indicator (FSI) [49–52] has been proposed to analyze how the rock elastic properties are affected by the different fluid saturation statuses. Whereas, in this study, a similar method is adopted to analyze the relative variations of rock physics attributes with respect to the changes in total/microcrack porosity, and it is defined as

$$SI = \frac{|\bar{A} - A_m|}{A_m}, \quad (8)$$

where A_m and \bar{A} represent the value of rock physics attribute at the minimal total (or microcrack) porosity and the average value of rock physics attribute within the considered range, respectively. Eleven attributes are considered, including density and the P- and S-wave velocities. The other eight are V_P/V_S , P-wave impedance (I_P), S-wave impedance (I_S), Poisson's ratio (ν), shear modulus (μ), the first Lamé constant (λ), $\lambda\rho$, and V_P/ρ .

Figure 10 shows the sensitivity indices to microcrack porosity at ultrasonic frequencies, where we observe that $\lambda\rho$, λ , ν , μ , and I_P are the most sensitive ones.

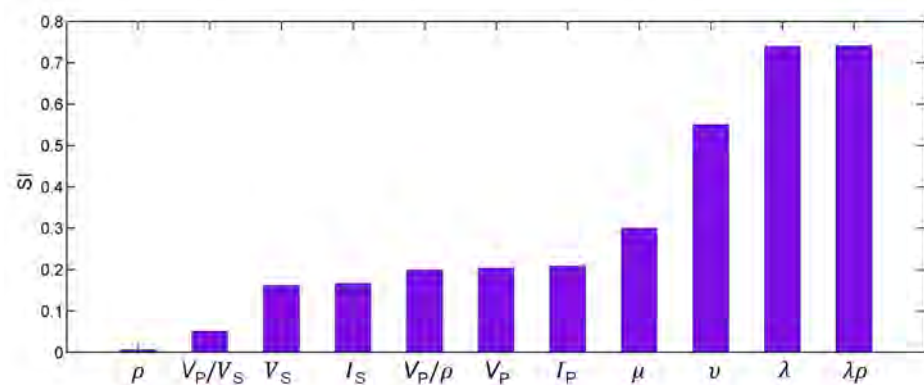


Figure 10. Sensitivity indices varying with the microcrack porosity.

The sensitivity analysis to total porosity is performed for the sonic log data, where we consider the gas-saturated layers of Well P. Figure 11 shows the results, where $\lambda\rho$, λ , ν , μ , and I_P are the most sensitive. In Figure 10, V_P/ρ , V_P , and I_P have a similar value while that of I_P is slightly higher than the values of V_P/ρ and V_P . However, it is obvious that in Figure 11 the value of I_P is higher than the values of V_P/ρ and V_P . According to Figures 10 and 11, ν and I_P are sensitive to both porosities and can be considered to build the rock-physics templates.

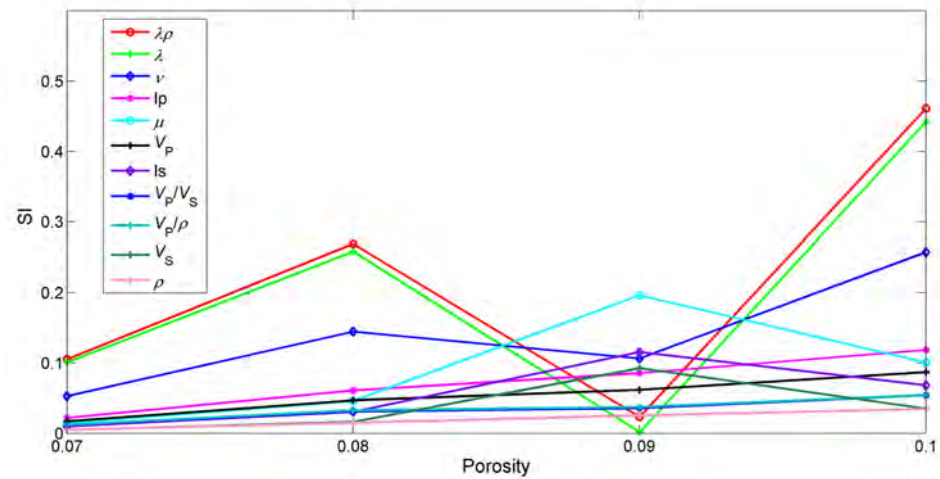


Figure 11. Sensitivity indices varying with the total porosity, based on data from Well P.

5. Rock-Physics Templates

5.1. Modeling

Figure 12 shows the RPTs with respect to total and microcrack porosities at ultrasonic and log frequencies, where the black and red curves isolines of total and microcrack porosities, respectively.

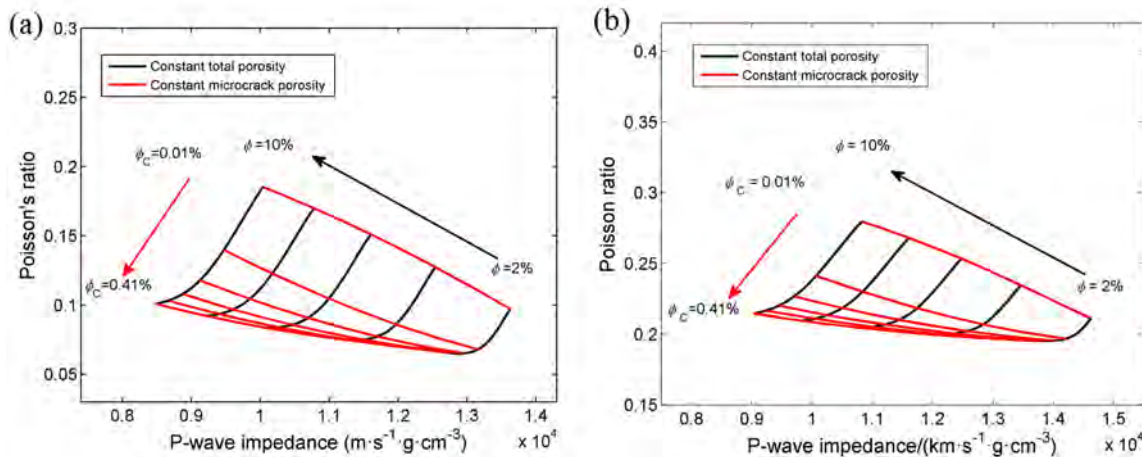


Figure 12. RPTs at ultrasonic (a) and sonic (b) frequencies.

5.2. Calibration

Ultrasonic and log data are used to calibrate the RPTs. Figure 13 displays an RPT at 1 MHz and the inclusion radius of 50 μm, where the color of the scatters indicates microcrack porosity, and the maximum value is 0.54%. The Poisson’s ratio gradually increases with decreasing microcrack porosity; the plot shows that the template is in agreement with the ultrasonic data.

Figure 14 shows an RPT at 10 kHz and the inclusion radius of 200 μm, where the color bar indicates total porosity (the data are from the log data of well P). Most of the data have a porosity greater than 4%. With the increasing porosity, Poisson’s ratio increases and P-wave impedance decreases, and the agreement between data and theory is good.

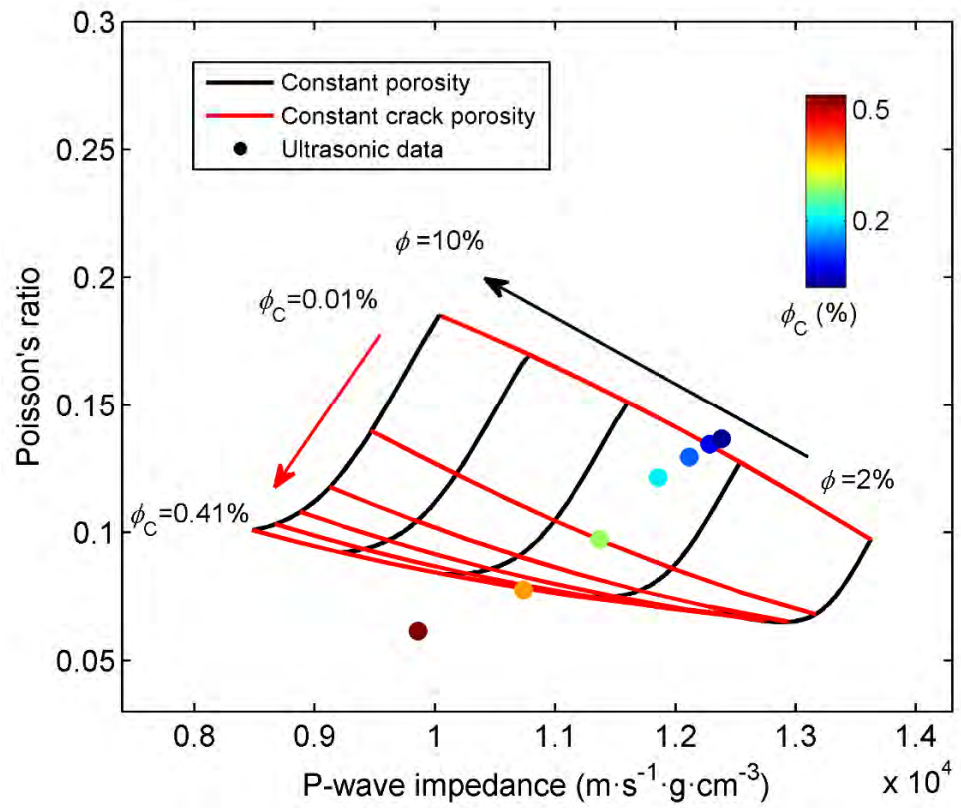


Figure 13. Ultrasonic data and corresponding RPT. The color bar indicates the microcrack porosity.

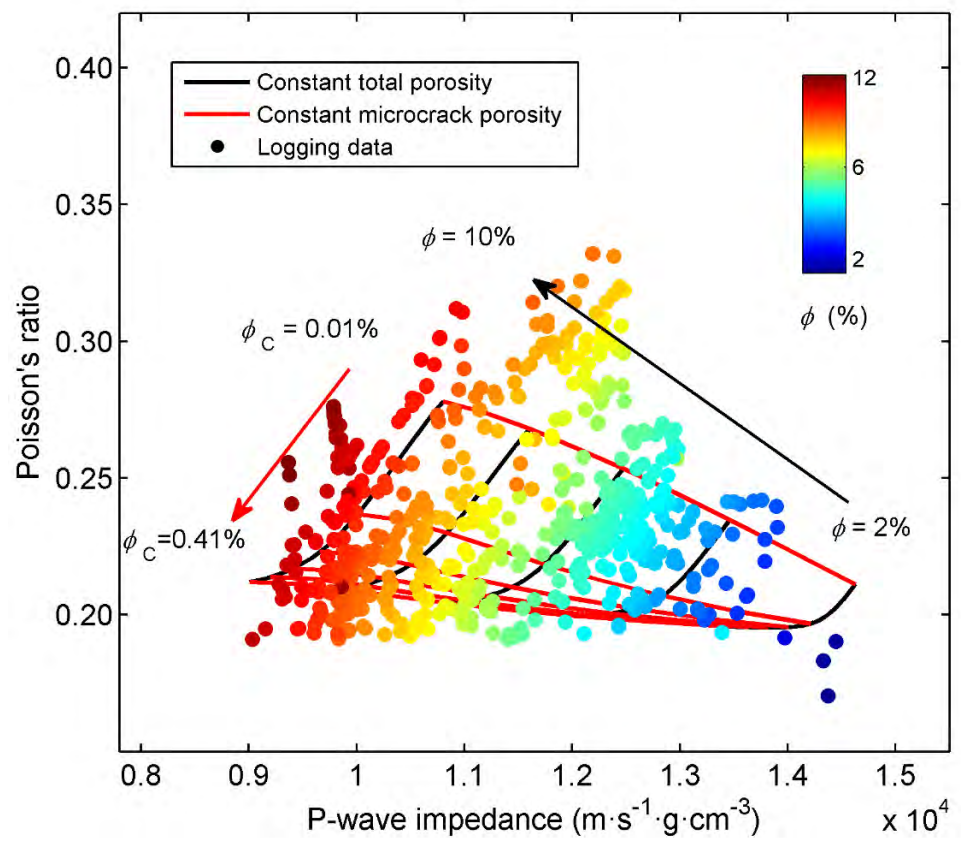


Figure 14. Log data and corresponding RPT. The color bar indicates the total porosity.

6. Microcrack Estimation

Based on approximated reflection coefficients [53], a pre-stack AVA inversion [54–56] is adopted to obtain the Poisson ratio and P-wave impedance and build the templates. Then, the microcrack porosity is estimated, with data points outside the template considered non-reservoir.

Figure 15 shows the P-wave impedance and Poisson's ratio obtained from a seismic survey line. Well M shows high P-wave impedances at the top and low P-wave impedances at the bottom of the target layer, and high Poisson's ratio in the middle. On the other hand, Well F shows the low impedance and Poisson's ratio. Figure 16 shows the total and microcrack porosities predicted for the survey. Both porosities are high at Well M and low at Well F. The gas production reports of wells M and F are $100.5 \times 10^4 \text{ m}^3$ per day and $4.4 \times 10^4 \text{ m}^3$ per day, respectively, indicating that the predictions are consistent with the reports.

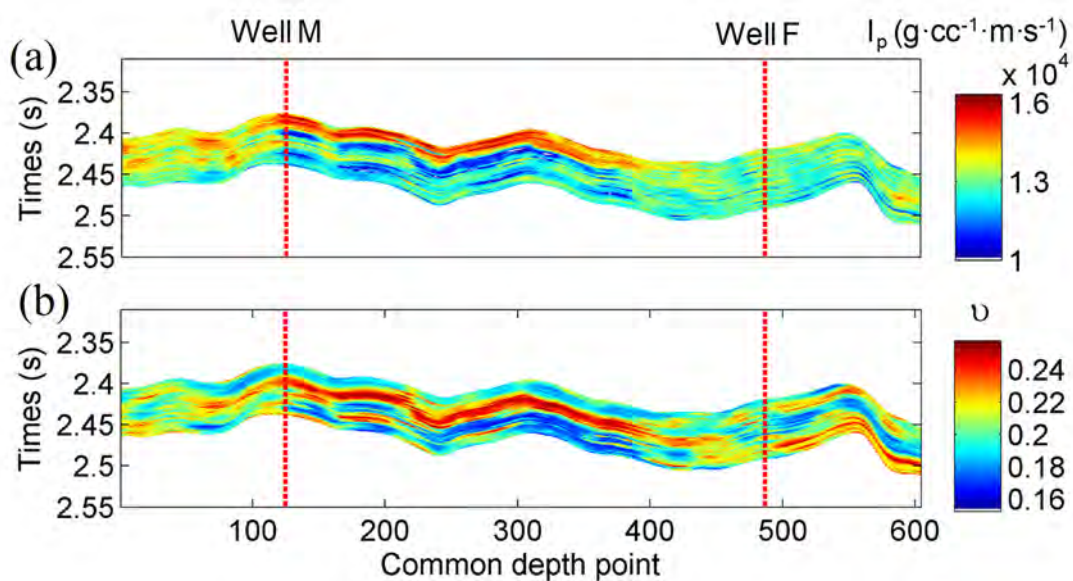


Figure 15. 2-D seismic profiles of P-wave impedance (a) and Poisson's ratio (b).

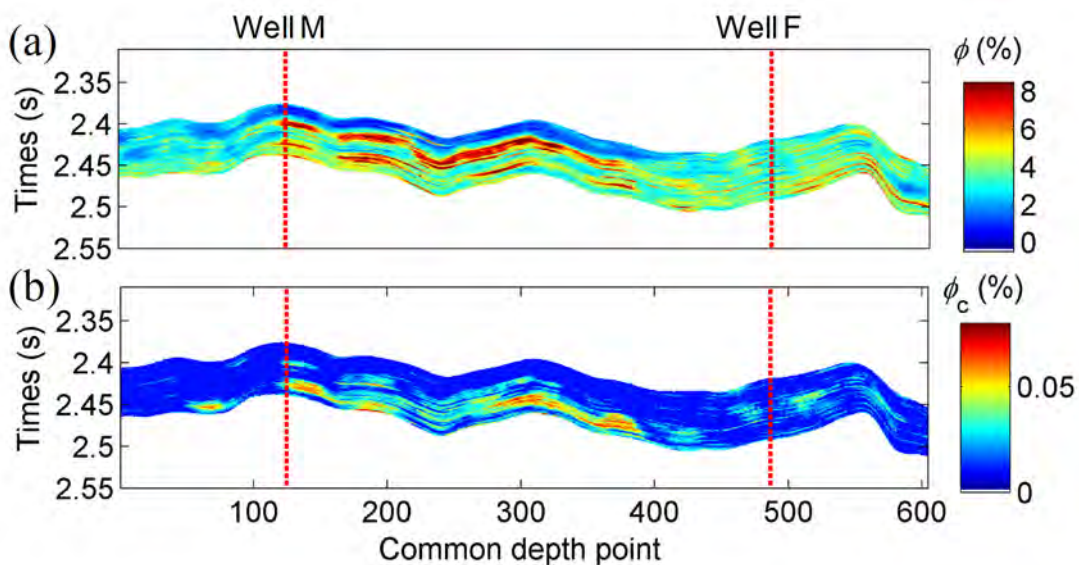


Figure 16. Inversion results of total (a) and microcrack (b) porosities corresponding to the data of Figure 15.

Figures 17 and 18 show results for another seismic survey line. Wells C and P show high P-wave impedances in the middle section, while Poisson's ratio is low throughout the target layer around Well C. This well exhibits low total and microcrack porosities (see Figure 18). Although Well P shows a higher total porosity, the microcrack porosity is low. Well J shows the best potential for gas production with high total and microcrack porosities. The reports show that Well C produced almost no gas with non-industrial gas production flow, while Wells P and J produce 2.14×10^4 and 6.4×10^4 m³ gas per day, respectively. The predictions of the porosities are consistent with the production status.

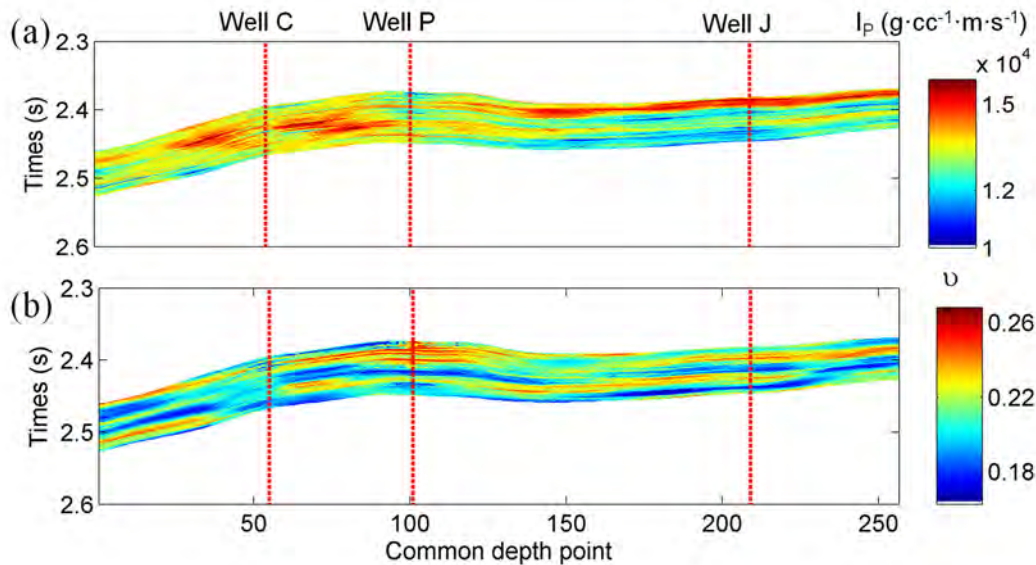


Figure 17. 2-D seismic profiles of P-wave impedance (a) and Poisson's ratio (b) corresponding to a second survey.

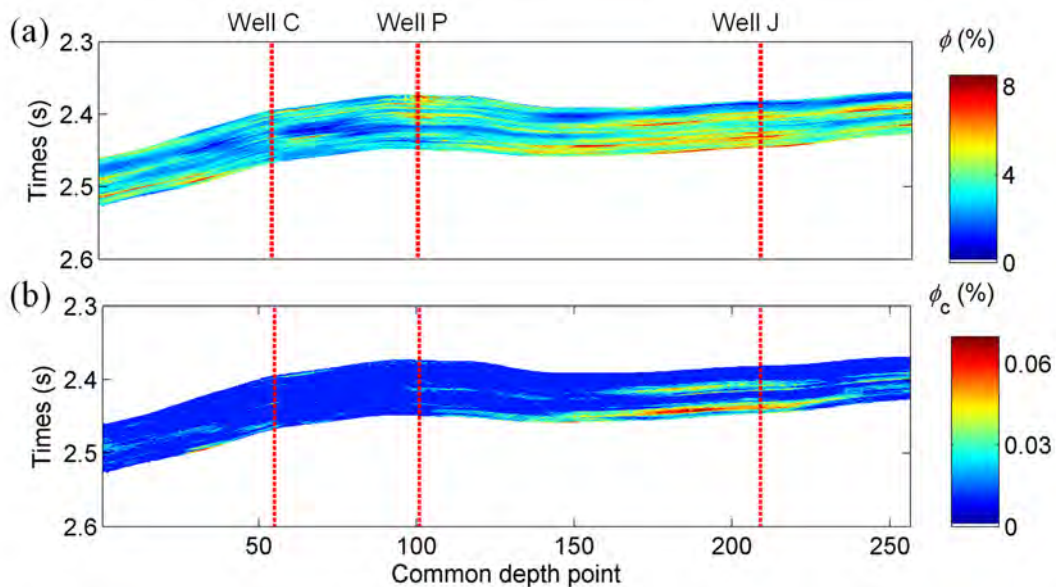


Figure 18. Inversion results of total (a) and microcrack (b) porosities, corresponding to the data of Figure 17.

3D seismic slices of the work area of ~ 471 km² are produced from the RPTs. According to the daily gas production rate, ten wells are classified into three categories, namely, extremely low (less than 1×10^4 m³), low ($1 \times 10^4 - 7 \times 10^4$ m³) and high (higher than 7×10^4 m³) gas production wells. Figures 19 and 20 show the corresponding maps of total and microcrack porosities, respectively.

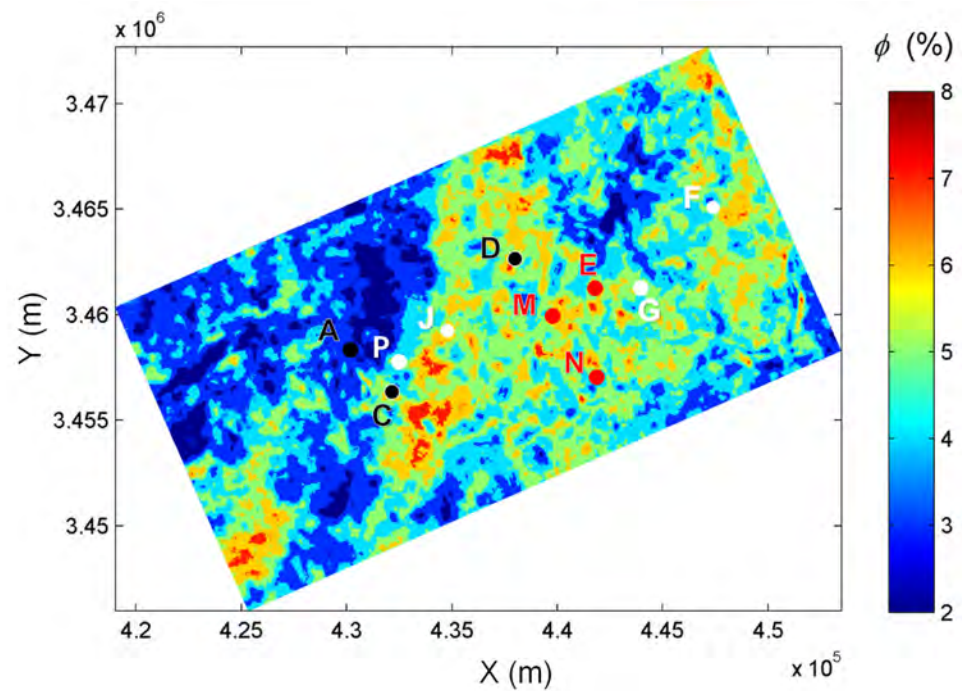


Figure 19. 3D slice of reservoir total porosity. Black, white, and red circles indicate extremely low, low, and high gas production wells, respectively.

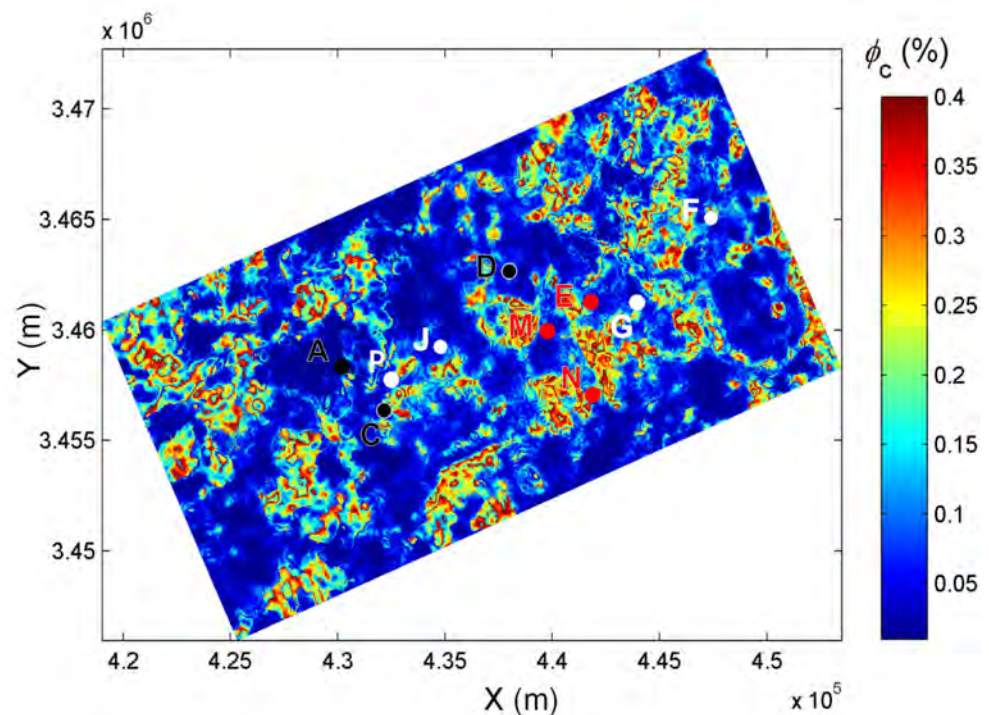


Figure 20. 3D slice of reservoir microcrack porosity. Black, white, and red circles indicate extremely low, low, and high gas production wells, respectively.

The predictions show that Well A is located in an area with extremely low total and microcrack porosities. The total porosity of Wells C and D are higher than that of Well A, but their microcrack porosities are low. Wells F, G, J, and P are located in an area with low total and microcrack porosities, whereas Wells E, N, and M show high total and microcrack porosities. According to the production test report, Well A is a water well with no gas

production, and Wells C and D produce almost no gas. The three wells are classified as the lowest production. Wells P, F, G, and J produce 2.14×10^4 , 4.4×10^4 , 5.76×10^4 , and 6.4×10^4 m³ gas per day, respectively, classified as low production. Wells E, N and M produce 17.66×10^4 , 25×10^4 , and 100.5×10^4 m³ gas per day, respectively, and are classified as high production. The predictions basically agree with the reports, so that the RPTs can discriminate between low and high gas production reservoirs.

7. Conclusions

This study uses rock-physics templates to estimate the total and microcrack porosities of tight sandstone gas reservoirs. The models are based on the poroelasticity theory to obtain the elastic attributes at different frequency bands, namely, how Poisson's ratio, velocity, and other relevant attributes are affected by those porosities. Ultrasonic experiments are performed under full water and gas saturations, showing that the wave velocities increase with effective pressure. When the rock is fully saturated with gas, the ratio between the P- and S-wave velocities increases with effective pressure, while for water, an opposite trend is observed.

A sensitivity analysis shows that P-wave impedance and Poisson's ratio are most sensitive to both porosities. The attributes are considered to build the templates which are calibrated with experimental and log data. Finally, the templates are applied to seismic data to estimate the porosities, indicating that the predictions are consistent with the gas production reports.

At present, the tight sandstone gas reservoirs of Sichuan Basin have contributed to the major proportion of the total gas production output of the petroleum industries in China. However, the tight sandstone reservoirs generally exhibit the characteristics of low porosity, low permeability, high heterogeneity, and deep burial. There are difficulties in the precise prediction and detailed description of high-quality reservoirs based on the traditional geophysical exploration methods. In this work, we propose a multiscale rock physics modeling method by incorporating the effects of microcrack porosity on rock physics attributes. A workflow is presented to establish the relationships between rock physical properties and seismic wave responses, based on which the prediction of microcrack porosity is achieved in the 3D seismic survey work area. The application of the method is effective as a case study.

The proposed method can be applied in rock physics modeling based on the elastic/seismic responses of reservoir rock. It may be affected by the problem of multiplicity of solutions in the parameter inversion and reservoir prediction. Further studies may incorporate the wave attenuation in rock physics modeling, so that more attributes will be available for validating and calibrating the templates, and the influence by the multiplicity of solutions can be alleviated. Furthermore, this paper is focused on the studies on tight gas sandstone reservoirs, and for the different types of complex reservoirs, the approach should be extended and adjusted to achieve effective applications. Specifically, for those tight/shale oil reservoirs, the viscoelasticity characteristics of fluid have to be analyzed and incorporated in rock physics modeling, so that some reasonable results can be obtained.

For future studies, the different sensitivity analysis methods should be included to analyze the interactions between different attributes with respect to rock basic properties. Furthermore, the multi-phases of different types of microcracks, mesopores and fractures need be considered to establish a more realistic rock model, with which the in situ reservoirs can be better described and simulated, in combination with the latest techniques of digital rock physics.

Author Contributions: Conceptualization, J.B. and R.H.; Data curation, T.C.; Formal analysis, C.R., J.B., J.M.C. and R.H.; Funding acquisition, J.B.; Investigation, J.B., J.M.C., T.C. and R.H.; Methodology, C.R., J.B. and J.M.C.; Project administration, J.B. and T.C.; Resources, T.C.; Supervision, J.B.; Validation, C.R. and J.M.C.; Writing—original draft, C.R. and J.B.; Writing—review & editing, J.B., J.M.C. and R.H. All authors have read and agreed to the published version of the manuscript.

Funding: This research was funded by National Natural Science Foundation of China, grant number 41974123, Jiangsu Province Outstanding Youth Fund Project, grant number BK20200021, and Strategic Priority Research Program of the Chinese Academy of Sciences, grant number XDA14010303.

Institutional Review Board Statement: Not applicable.

Informed Consent Statement: Not applicable.

Data Availability Statement: The data relevant with this study can be accessed by contacting the corresponding author.

Acknowledgments: The authors are grateful to the National Natural Science Foundation of China (Grant no. 41974123), the Jiangsu Province Outstanding Youth Fund Project (Grant no. BK20200021), and the Strategic Priority Research Program of the Chinese Academy of Sciences (Grant no. XDA14010303).

Conflicts of Interest: The authors declare no conflict of interest.

Abbreviations

AVO	Amplitude variation with offset
BR	Biot–Rayleigh
DEM	Differential equivalent medium
RPT	Rock physics template
FSI	Fluid sensitivity indicator

Appendix A

The Biot–Rayleigh theory

The BR dispersion equation [28] yields the complex wave number k ,

$$\begin{vmatrix} a_{11}k^2 + b_{11} & a_{12}k^2 + b_{12} & a_{13}k^2 + b_{13} \\ a_{21}k^2 + b_{21} & a_{22}k^2 + b_{22} & a_{23}k^2 + b_{23} \\ a_{31}k^2 + b_{31} & a_{32}k^2 + b_{32} & a_{33}k^2 + b_{33} \end{vmatrix} = 0, \quad (\text{A1})$$

where

$$\begin{aligned} a_{11} &= A + 2N + i(Q_2\phi_1 - Q_1\phi_2)x_1, & b_{11} &= -\rho_{11}\omega^2 + i\omega(b_1 + b_2), \\ a_{12} &= Q_1 + i(Q_2\phi_1 - Q_1\phi_2)x_2, & b_{12} &= -\rho_{12}\omega^2 - i\omega b_1, \\ a_{13} &= Q_2 + i(Q_2\phi_1 - Q_1\phi_2)x_3, & b_{13} &= -\rho_{13}\omega^2 - i\omega b_2, \\ a_{21} &= Q_1 - iR_1\phi_2x_1, & b_{21} &= -\rho_{12}\omega^2 - i\omega b_1, \\ a_{22} &= R_1 - iR_1\phi_2x_2, & b_{22} &= -\rho_{22}\omega^2 + i\omega b_1, \\ a_{23} &= -iR_1\phi_2x_3, & b_{23} &= 0, \\ a_{31} &= Q_2 + iR_2\phi_1x_1, & b_{31} &= -\rho_{13}\omega^2 - i\omega b_2, \\ a_{32} &= iR_2\phi_1x_2, & b_{32} &= 0, \\ a_{33} &= R_2 + iR_2\phi_1x_3, & b_{33} &= -\rho_{33}\omega^2 + i\omega b_2, \end{aligned} \quad (\text{A2})$$

and

$$\begin{aligned} x_1 &= i(\phi_2Q_1 - \phi_1Q_2)/Z, & x_2 &= i\phi_2R_1/Z, & x_3 &= -i\phi_1R_2/Z, \\ Z &= \frac{i\omega\eta\phi_1^2\phi_2\phi_{20}R_0^2}{3\kappa_{10}} - \frac{\rho_f\omega^2R_0^2\phi_1^2\phi_2\phi_{20}}{3\phi_{10}} - (\phi_2^2R_1 + \phi_1^2R_2), \end{aligned} \quad (\text{A3})$$

where ω is the angular frequency; ϕ_{10} and ϕ_{20} are the local porosities of intergranular pores and microcracks, respectively; and ϕ_1 and ϕ_2 are the corresponding absolute porosities. ρ_f , η , and κ_{10} are the fluid density, the fluid viscosity, and rock permeability, respectively; A , N , Q_1 , R_1 , Q_2 , and R_2 are elastic parameters; R_0 is the radius of inclusion; ρ_{11} , ρ_{12} , ρ_{13} ,

ρ_{22} , and ρ_{33} are density parameters; and b_1 and b_2 are Biot dissipative parameters. The expressions for all these quantities can be found in [28,29].

References

1. Yan, X.-F.; Yao, F.-C.; Cao, H.; Ba, J.; Hu, L.-L.; Yang, Z.-F. Analyzing the mid-low porosity sandstone dry frame in central Sichuan based on effective medium theory. *Appl. Geophys.* **2011**, *8*, 163–170. [[CrossRef](#)]
2. Li, Y.; Tang, D.Z.; Wu, P.; Niu, X.L.; Wang, K.; Qiao, P.; Wang, Z.S. Continuous unconventional natural gas accumulations of Carboniferous-Permian coal-bearing strata in the Linxing area, northeastern Ordos basin, China. *J. Nat. Gas Sci. Eng.* **2016**, *36*, 314–327. [[CrossRef](#)]
3. Zhu, R.; Zou, C.; Zhang, N.; Wang, X.; Cheng, R.; Liu, L.; Zhou, C.; Song, L. Diagenetic fluids evolution and genetic mechanism of tight sandstone gas reservoirs in Upper Triassic Xujiahe Formation in Sichuan Basin, China. *Sci. China Ser. D Earth Sci.* **2008**, *51*, 1340–1353. [[CrossRef](#)]
4. Wang, J.L.; Feng, L.Y.; Steve, M.; Tang, X.; Gail, T.E.; Mikael, H. China's unconventional oil: A review of its resources and outlook for long-term production. *Energy* **2015**, *82*, 31–42. [[CrossRef](#)]
5. Yang, K.M.; Zhu, H.Q.; Ye, J.; Zhang, K.G.; Ke, G.M. *Geological Characteristics of Tight Sandstone Gas Reservoirs in West Sichuan Basin*; Science Press: Beijing, China, 2012.
6. Luo, Y.; Huang, H.; Jakobsen, M.; Yang, Y.; Zhang, J.; Cai, Y. Prediction of porosity and gas saturation for deep-buried sandstone reservoirs from seismic data using an improved rock-physics model. *Acta Geophys.* **2019**, *67*, 557–575. [[CrossRef](#)]
7. Carcione, J.M. *Wave Fields in Real Media: Theory and Numerical Simulation of Wave Propagation in Anisotropic, Anelastic, Porous and Electromagnetic Media*; Elsevier: Amsterdam, The Netherlands, 2014.
8. Wang, L.; Zhao, N.; Sima, L.; Meng, F.; Guo, Y. Pore Structure Characterization of the Tight Reservoir: Systematic Integration of Mercury Injection and Nuclear Magnetic Resonance. *Energy Fuels* **2018**, *32*, 7471–7484. [[CrossRef](#)]
9. Wang, X.X.; Hou, J.G.; Song, S.H.; Wang, D.M.; Gong, L.; Ma, K.; Liu, L.M.; Li, Y.Q.; Yan, L. Combining pressure-controlled porosimetry and rate-controlled porosimetry to investigate the fractal characteristics of full-range pores in tight oil reservoirs. *J. Pet. Sci. Eng.* **2018**, *171*, 353–361. [[CrossRef](#)]
10. Stroker, T.M.; Harris, N.; Elliott, W.C.; Wampler, J.M. Diagenesis of a tight gas sand reservoir: Upper Cretaceous Mesaverde Group, Piceance Basin, Colorado. *Mar. Pet. Geol.* **2013**, *40*, 48–68. [[CrossRef](#)]
11. Liu, L.; Tang, D.Z.; Wo, Y.J.; Liu, L.H.; Sun, W.; Liu, H.M.; Yekikang, M.Q. Favorable area prediction of tight sandstone: A case study of the He8 formation in the Kangning area, Eastern Ordos Basin, China. *J. Pet. Sci. Eng.* **2019**, *175*, 430–443.
12. Vernik, L.; Kachanov, M. Modeling elastic properties of siliciclastic rocks. *Geophysics* **2010**, *75*, E171–E182. [[CrossRef](#)]
13. Hudson, J.A. A higher order approximation to the wave propagation constants for a cracked solid. *Geophys. J. Int.* **1986**, *87*, 265–274. [[CrossRef](#)]
14. Smith, T.M.; Sayers, C.; Sondergeld, C.H. Rock properties in low-porosity/low-permeability sandstones. *Geophysics* **2009**, *28*, 48–59. [[CrossRef](#)]
15. Yoon, H.-K. Relationship between Aspect Ratio and Crack Density in Porous-Cracked Rocks Using Experimental and Optimization Methods. *Appl. Sci.* **2020**, *10*, 7147. [[CrossRef](#)]
16. Cheng, W.; Ba, J.; Ma, R.P.; Zhang, L. A study on the effects of pressure and fluid on rock pore structure and anelasticity: Theoretical model and experimental measurement. *Chin. J. Geophys.* **2020**, *63*, 4517–4527. (In Chinese)
17. Zhang, L.; Ba, J.; Carcione, J.M.; Fu, L.-Y. Differential poroelasticity model for wave dissipation in self-similar rocks. *Int. J. Rock Mech. Min. Sci.* **2020**, *128*, 104281. [[CrossRef](#)]
18. Zhang, L.; Ba, J.; Carcione, J.M. Wave Propagation in Infinituple-Porosity Media. *J. Geophys. Res. Solid Earth* **2021**, *126*, e2020JB021266. [[CrossRef](#)]
19. Avseth, P.A.; Odegaard, E. Well log and seismic data analysis using rock physics templates. *First Break* **2004**, *22*, 37–43. [[CrossRef](#)]
20. Avseth, P.; Mukerji, T.; Mavko, G. *Quantitative Seismic Interpretation: Applying Rock Physics Tools to Reduce Interpretation Risk*; Cambridge University Press: Cambridge, MA, USA, 2005.
21. Xin, G.; Han, D. Lithology and fluid differentiation using a rock physics template. *Lead. Edge* **2009**, *28*, 60–65.
22. Michel, K. Rock physics driven inversion: The importance of workflow. *First Break* **2010**, *28*, 68–81.
23. Gupta, S.D.; Chatterjee, R.; Farooqui, M.Y. Rock physics template (RPT) analysis of well logs and seismic data for lithology and fluid classification in Cambay Basin. *Acta Diabetol.* **2012**, *101*, 1407–1426. [[CrossRef](#)]
24. Ba, J.; Cao, H.; Carcione, J.M.; Tang, G.; Yan, X.-F.; Sun, W.-T.; Nie, J.-X. Multiscale rock-physics templates for gas detection in carbonate reservoirs. *J. Appl. Geophys.* **2013**, *93*, 77–82. [[CrossRef](#)]
25. Carcione, J.M.; Avseth, P. Rock-physics templates for clay-rich source rocks. *Geophysics* **2015**, *80*, D481–D500. [[CrossRef](#)]
26. Liu, Q.; Yin, X.; Li, C. Fluid discrimination based on rock physics templates. *J. Geophys. Eng.* **2015**, *12*, 830–838. [[CrossRef](#)]
27. Pang, M.Q.; Ba, J.; Carcione, J.M.; Vesnaver, A.; Ma, R.P.; Chen, T.S. Analysis of attenuation rock-physics template of tight sandstones: Reservoir microcrack prediction. *Chin. J. Geophys.* **2020**, *63*, 4205–4219.
28. Ba, J.; Carcione, J.M.; Nie, J.X. Biot-Rayleigh theory of wave propagation in double-porosity media. *J. Geophys. Res. Space Phys.* **2011**, *116*, 06202. [[CrossRef](#)]
29. Ba, J.; Xu, W.; Fu, L.-Y.; Carcione, J.M.; Zhang, L. Rock anelasticity due to patchy saturation and fabric heterogeneity: A double double-porosity model of wave propagation. *J. Geophys. Res. Solid Earth* **2017**, *122*, 1949–1976. [[CrossRef](#)]

30. Liu, J.L.; Liu, Z.Q.; Xiao, K.H.; Huang, Y.Q.; Jin, W.J. Characterization of favorable lithofacies in tight sandstone reservoirs and its significance for gas exploration and exploitation: A case study of the 2~(nd) Member of Triassic Xujiahe Formation in the Xinchang area, Sichuan Basin. *Pet. Explor. Dev.* **2020**, *47*, 50–61. [[CrossRef](#)]
31. Yang, P.; Zhang, L.; Liu, K.; Cao, B.; Gao, J.; Qiu, G. Diagenetic history and reservoir evolution of tight sandstones in the second member of the Upper Triassic Xujiahe Formation, western Sichuan Basin, China. *J. Pet. Sci. Eng.* **2021**, *201*, 108451. [[CrossRef](#)]
32. Wu, D.; Liu, S.; Chen, H.; Lin, L.; Yu, Y.; Xu, C.; Pan, B. Investigation and prediction of diagenetic facies using well logs in tight gas reservoirs: Evidences from the Xu-2 member in the Xinchang structural belt of the western Sichuan Basin, western China. *J. Pet. Sci. Eng.* **2020**, *192*, 107326. [[CrossRef](#)]
33. Wang, Q.; Chen, D.; Gao, X.; Wang, F.; Li, J.; Liao, W.; Wang, Z.; Xie, G. Microscopic pore structures of tight sandstone reservoirs and their diagenetic controls: A case study of the Upper Triassic Xujiahe Formation of the Western Sichuan Depression, China. *Mar. Pet. Geol.* **2020**, *113*, 104119. [[CrossRef](#)]
34. Liu, C.; Pei, S.J.; Guo, Z.Q.; Fu, W.; Zhang, Y.S.; Liu, X.W. Seismic AVO Simulation and Analysis in Heterogeneous Media. *J. Jilin Univ. Earth Sci. Ed.* **2018**, *48*, 1512–1521.
35. Rutherford, S.R.; Williams, R.H. Amplitude-Versus-Offset Variations in gas sands. *Geophysics* **1989**, *54*, 680–688. [[CrossRef](#)]
36. Castagna, J.P.; Swan, H.W. Principles of AVO cross plotting. *Lead. Edge* **1997**, *16*, 337–342. [[CrossRef](#)]
37. Voigt, W. Lehrbuch der Kristallphysik. *Teubner Leipz.* **1910**, *1928*, 739.
38. Reuss, A. Calculation of the flow limits of mixed crystals on the basis of the plasticity of monocrystals. *Z. Angew. Mathematik* **1929**, *9*, 49–58. [[CrossRef](#)]
39. Hill, R. The Elastic Behaviour of a Crystalline Aggregate. *Proc. Phys. Soc. Sect. A* **1952**, *65*, 349–354. [[CrossRef](#)]
40. Berryman, J.G. Single-scattering approximations for coefficients in Biot's equations of poroelasticity. *J. Acoust. Soc. Am.* **1992**, *91*, 551–571. [[CrossRef](#)]
41. Berryman, J.G. Long-wavelength propagation in composite elastic media II. Ellipsoidal inclusions. *J. Acoust. Soc. Am.* **1980**, *68*, 1820–1831. [[CrossRef](#)]
42. Batzle, M.; Wang, Z. Seismic properties of pore fluids. *Geophysics* **1992**, *57*, 1396–1408. [[CrossRef](#)]
43. Guo, M.-Q.; Fu, L.-Y.; Ba, J. Comparison of stress-associated coda attenuation and intrinsic attenuation from ultrasonic measurements. *Geophys. J. Int.* **2009**, *178*, 447–456. [[CrossRef](#)]
44. Shapiro, S. Elastic piezosensitivity of porous and fractured rocks. *Geophysics* **2003**, *68*, 482–486. [[CrossRef](#)]
45. Pervukhina, M.; Gurevich, B.; Dewhurst, D.; Siggins, A.F. Applicability of velocity-stress relationships based on the dual porosity concept to isotropic porous rocks. *Geophys. J. Int.* **2010**, *181*, 1473–1479. [[CrossRef](#)]
46. Yin, H.J.; Zhao, J.G.; Tang, G.Y.; Zhao, L.M.; Ma, X.Y.; Wang, S.X. Pressure and fluid effect on frequency-dependent elastic moduli in fully saturated tight sandstone. *J. Geophys. Res. Solid Earth* **2017**, *122*, 8925–8942. [[CrossRef](#)]
47. Cheng, W.; Ba, J.; Carcione, J.M.; Pang, M.; Wu, C. Estimation of the Pore Microstructure of Tight-Gas Sandstone Reservoirs with Seismic Data. *Front. Earth Sci.* **2021**, *9*, 1–12. [[CrossRef](#)]
48. Amini, A.; Abdollahi, A.; Hariri-Ardebili, M.; Lall, U. Copula-based reliability and sensitivity analysis of aging dams: Adaptive Kriging and polynomial chaos Kriging methods. *Appl. Soft Comput.* **2021**, *109*, 107524. [[CrossRef](#)]
49. Pei, F.-G.; Zou, C.-C.; He, T.; Shi, G.; Qiu, G.-G.; Ren, K.-Y. Fluid sensitivity study of elastic parameters in low-medium porosity and permeability reservoir rocks. *Appl. Geophys.* **2010**, *7*, 1–9. [[CrossRef](#)]
50. Guo, Y.; Ma, H.; Ba, J.; Yu, H.; Long, C. Impact of data distribution on fluid sensitivity analysis: A quantitative investigation. *J. Appl. Geophys.* **2015**, *119*, 1–15. [[CrossRef](#)]
51. Zeng, Q.J.; Guo, Y.; Jiang, R.; Ba, J.; Ma, H.D.; Liu, J. Fluid sensitivity of rock physics parameters in reservoirs: Quantitative analysis. *J. Seism. Explor.* **2017**, *26*, 125–140.
52. Ma, R.; Ba, J.; Carcione, J.; Lebedev, M.; Wang, C. Experimental Study on Petrophysical Properties as a Tool to Identify Pore Fluids in Tight-Rock Reservoirs. *Front. Earth Sci.* **2021**, *9*, 334. [[CrossRef](#)]
53. Aki, K.; Richards, P.G. *Quantitative Seismology*; W. H. Freeman & Co.: New York, NY, USA, 1980.
54. Buland, A.; Omre, H. Bayesian linearized AVO inversion. *Geophysics* **2003**, *68*, 185–198. [[CrossRef](#)]
55. Luo, C.; Ba, J.; Carcione, J.M.; Huang, G.; Guo, Q. Joint PP and PS Pre-stack Seismic Inversion for Stratified Models Based on the Propagator Matrix Forward Engine. *Surv. Geophys.* **2020**, *41*, 987–1028. [[CrossRef](#)]
56. Luo, C.; Huang, G.; Chen, X.; Chen, Y. Registration-Free Multicomponent Joint AVA Inversion Using Optimal Transport. *IEEE Trans. Geosci. Remote. Sens.* **2021**, *99*, 1–13. [[CrossRef](#)]